Article

A Study to Improve the Performance of Mixed Cation–Halide Perovskite-Based UVC Photodetectors

Ga In Choi [ID] and Hyung Wook Choi *

Department of Electrical Engineering, Gachon University, 1342 Seongnam-daero, Seongnam-si 13120, Korea; gana034@gachon.ac.kr
* Correspondence: chw@gachon.ac.kr; Tel.: +82-31-750-5562

Abstract: Photodetectors convert optical signals into electrical signals and demonstrate application potential in various fields, such as optical communication, image detection, environmental monitoring, and optoelectronics. In this study, a mixed cation–halide perovskite-based ultraviolet C photodetector was fabricated using a solution process. The higher the mobility of the perovskite carrier, which is one of the factors affecting the performance of electronic power devices, the better the carrier diffusion. The on/off ratio and responsivity indicate the sensitivity of the response, and together with the detectivity and external quantum efficiency, these parameters demonstrate the performance of the detector. The detector fabricated in this study exhibited a mobility of $202.2 \ cm^2/Vs$ and a high on/off ratio of $10^5\%$ at a -2 V bias, under 254 nm light irradiation with an intensity of $0.6 \ mW/cm^2$. The responsivity, detectivity, and external quantum efficiency of the as-fabricated detector were 5.07 mA/W, 5.49×10^{11} Jones, and 24.8%, respectively. These findings demonstrate that the solution process employed in this study is suitable for the fabrication of mixed cation–halide perovskites which show immense potential for use as photodetectors.

Keywords: mixed cation; mixed halide; perovskite device; UVC sensor; photodetector

1. Introduction

A photodetector is a device that converts an optical signal into an electrical signal and exhibits a high detection rate, allowing the detection of weak optical signals [1,2]. Photodetectors have been used in various fields, such as optical communication, image detection, and environmental monitoring [3–6]. In particular, ultraviolet C (UVC) photodetectors operating in the 280–100 nm region have been intensively studied owing to their ability to precisely detect weak signals [7]. UV rays can be divided into three categories according to wavelength: UVA (400–320 nm), UVB (320–280 nm), and UVC (280–100 nm) [8]. UVC radiation is largely absorbed by the ozone layer [8]. However, UVC radiation is emitted by artificial light sources, such as mercury lamps, UV germicidal bulbs, and arc discharges [9–12], and is harmful to human health. Additionally, it is the cause of many safety issues in industrial facilities [13,14]. Therefore, it is essential to develop a system to detect UVC radiation in order to increase worker safety and reduce facility management costs.

When fabricating a UVC photodetector, it is necessary to consider whether a low-temperature and simple process is possible. This is because it is essential to develop sustainable electronic devices to reduce the impacts on the environment of energy consumption and waste [15,16]. Low energy processes make it possible to produce more eco-friendly devices [17].

Various characteristics of photodetectors, such as stability, light absorption, carrier mobility, band gap, reactivity, detectability, and on/off ratio, are dependent on the material composition. Accordingly, photodetectors comprising various materials have been investigated [1]. Photodetectors comprising materials such as group III–V compound semiconductors, organic polymers, and silicon have been fabricated [2], and narrow bandgap Si

diode sensors equipped with UV filters have been developed [14]. However, photodetectors containing these materials are expensive and require complex fabrication processes [18]. Additionally, Si diodes offer limited UVC sensitivity because the photogenerated carriers cannot easily reach the depletion layer of the semiconductor [14].

Recently, perovskites have attracted attention in the field of optoelectronic devices, such as light-emitting diodes and solar cells [19,20], owing to their tunable bandgaps, large light absorption, and long diffusion lengths (L_D values) [21]. In addition, the solution process fabrication of perovskites is simple and economical [22,23].

Methylammonium (MA) and formamidinium (FA) cations are commonly used in perovskite light absorption layers [21,24], and methylammonium lead halide ($MAPbX_3$) has attracted attention as a material for developing hybrid organic–inorganic perovskites owing to its excellent photoelectric properties [25]. However, $MAPbX_3$ perovskites exhibit phase instability at high temperatures and are more sensitive to moisture and light than FA-based perovskites, leading to the separation of halide components [26,27]. Formamidinium lead halides ($FAPbX_3$) have a higher thermal stability than $MAPbX_3$ [24,28]; however, $FAPbI_3$ exhibits low phase stability at room temperature and can be converted from the "black" α-phase to the "yellow" δ-phase [29,30].

Therefore, perovskite materials comprising only pure cation MA or FA are not optimal owing to their instability. However, the incorporation of MA^+ into $FAPbI_3$-based perovskite via the crystal nucleation mechanism prevents the formation of δ-$FAPbI_3$ [31], and this stabilization improves performance [32]. Additionally, the iodide can be partially substituted with a bromide to improve the performance of FA/MA mixed cation perovskites, as the addition of a small amount of Br^- improves phase stability [33,34]. The partial substitution of I^- with Br^- maintains excellent light absorption properties and increases the carrier lifetime and mobility [25]. The mixed cation–halide perovskite features improvements in crystallinity, stability, and electrical properties, such as light absorption, photocurrent, carrier mobility, and L_D. Therefore, mixed cation–halide perovskites have potential as materials for use in high performance UVC photodetectors with a low energy process and cost.

In this study, $(FAPbI_3)_{1-x}(MAPbBr_3)_x$ (x = 0, 0.03, 0.05, 0.07, and 0.1) photodetectors were fabricated by adding $MAPbBr_3$ to $FAPbI_3$, considering the low thermal stability of MABr at different mol% ratios. The fabricated mixed cation–halide perovskite-based photodetector exhibited improved stability, photocurrent, and responsiveness compared with a pure $FAPbI_3$ photodetector. The performance of the photodetector was determined by investigating various characteristics, including responsivity, detectivity, carrier mobility, light absorption, dark environment, and current under 254 nm irradiation. The responsivity, detectivity, and external quantum efficiency (EQE) of the as-fabricated $(FAPbI_3)_{1-x}(MAPbBr_3)_x$-based photodetectors were 5.07 mA/W, 5.49×10^{11} Jones, and 24.8%, respectively, under 254 nm light irradiation with a -2 V bias and 0.6 mW/cm² intensity. This value is more than six times larger than that of a pure $FAPbI_3$ photodetector. These results show that the mixed cation–halide perovskite provides improved optical properties compared with the pure $FAPbI_3$ perovskite, and therefore, is a promising candidate for UVC photodetector fabrication.

2. Materials and Methods

2.1. Materials

The materials and chemicals used were as follows: quartz indium tin oxide (ITO) patterned glass (etching interval: 10 μm) with a thickness of 150 nm, lead (II) iodide (99.999% trace metal basis), *N*,*N*-dimethylformamide (DMF, 99.8%), toluene (99.8%), dimethyl sulfoxide (DMSO, 99.7%), FA iodide (FAI), MA iodide (MAI), and MA chloride (MACl).

2.2. Preparation of $(FAPbI_3)_{1-x}(MAPbBr_3)_x$-Based Perovskite Photodetector

Figure 1a shows a schematic diagram of a metal-semiconductor-metal-type photodetector, and Figure 1b illustrates the fabrication process. An ITO quartz substrate etched at

10 μm intervals was used to prepare the $(FAPbI_3)_{1-x}(MAPbBr_3)_x$ films. To remove organic matter, the ITO quartz substrate was ultrasonically cleaned using a neutral detergent, water, acetone, ethanol, and distilled water for 20 min each. After drying in an oven at 80 °C for 20 min, UV-ozone treatment was performed for 30 min to further remove moisture. A $(FAPbI_3)_{1-x}(MAPbBr_3)_x$ solution was prepared by dissolving PbI_2 and $PbBr_2$ (1.4 M), FAI, and MABr (1.4 M) in DMF (1 mL), which was then mixed with 100 μL of DMSO. The perovskite precursor solution was then stirred for 1 h at 23 °C. MACl was then added, up to 40 mol% of FAI, and the solution was further stirred for 30 min. The solution was deposited on a quartz substrate via spin coating at 4000 rpm for 20 s, over which toluene was dropped for the last 10 s. After spin-coating, the thin film was annealed at 150 °C for 15 min.

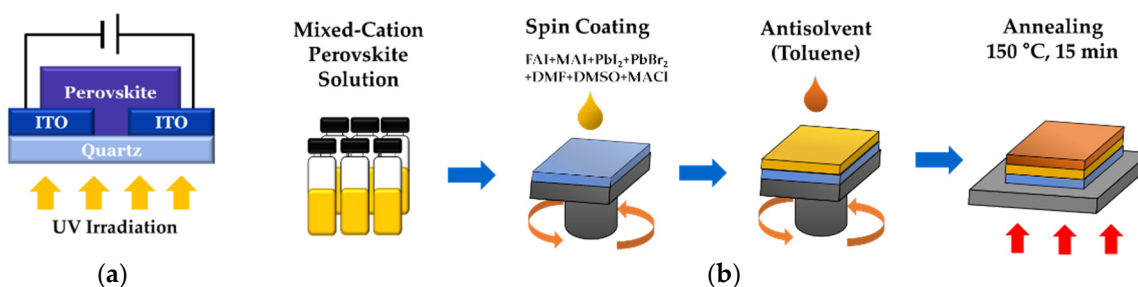**Figure 1.** (**a**) Schematic and (**b**) fabrication process of the $(FAPbI_3)_{1-x}(MAPbBr_3)_x$ photodetector.

2.3. Device Characterization

The crystal structure of the perovskite film was investigated using X-ray diffraction (XRD, DMAX 2200, Rigaku, Japan) with a scan rate of 3.00°/min. The morphology of the photodetector surface was observed using scanning electron microscopy (SEM, S-4700, Hitachi, Japan). The light absorptivity of the device was measured using UV-visible (UV-vis) spectroscopy (UV-vis 8453, Agilent, Santa Clara, CA, USA). The electrical response of the perovskite photodetector was measured with a combined source and measurement meter (Source Measure Unit, Keithley Instruments, Cleveland, OH, USA) and a UV lamp (6 W, 254 nm) (VL-6.LC, Vilber Lourmat, Marne-la-Vallée, France) under 254 nm irradiation.

3. Results and Discussion

Figure 2a shows the XRD patterns of the fabricated perovskites. $(FAPbI_3)_{1-x}(MAPbBr_3)_x$ films were fabricated with different ratios of x (x = 0, 0.03, 0.05, 0.07, and 0.1). Several characteristic perovskite peaks were observed in the XRD patterns. The peaks at ~11.7°, ~12.7°, and ~14.0° of the diffractogram were assigned to the δ-$FAPbI_3$, PbI_2, and α-$FAPbI_3$ phases, respectively. Pure $FAPbI_3$ (x = 0) exhibited the highest δ-$FAPbI_3$ peak intensity and possessed low phase stability owing to the high concentration of δ-$FAPbI_3$. As the $MAPbBr_3$ content of the film increased, δ-$FAPbI_3$ was converted to α-$FAPbI_3$ [25], which decreased the peak intensity of δ-$FAPbI_3$. However, the reduction of the δ-$FAPbI_3$ content did not improve the crystallinity of the all perovskite films. Although the α-$FAPbI_3$ peak intensity of the $(FAPbI_3)_{1-x}(MAPbBr_3)_x$ film increased up to x = 0.05, it started to decrease at x = 0.07 and exhibited the smallest peak intensity at x = 0.1. This is because the low thermal stability of MABr led to the degradation of $MAPbBr_3$. As the "black" α-$FAPbI_3$ phase is thermodynamically stable above 150 °C, $FAPbI_3$ was annealed at 150 °C [32]. However, MA^+ has low thermal stability [26], and therefore, at high temperatures, a portion of $MAPbBr_3$ thermally decomposes to form a PbI_2 phase [32,35]. The highest PbI_2 peak intensity was observed when x = 0.1, as shown in Figure 2a.
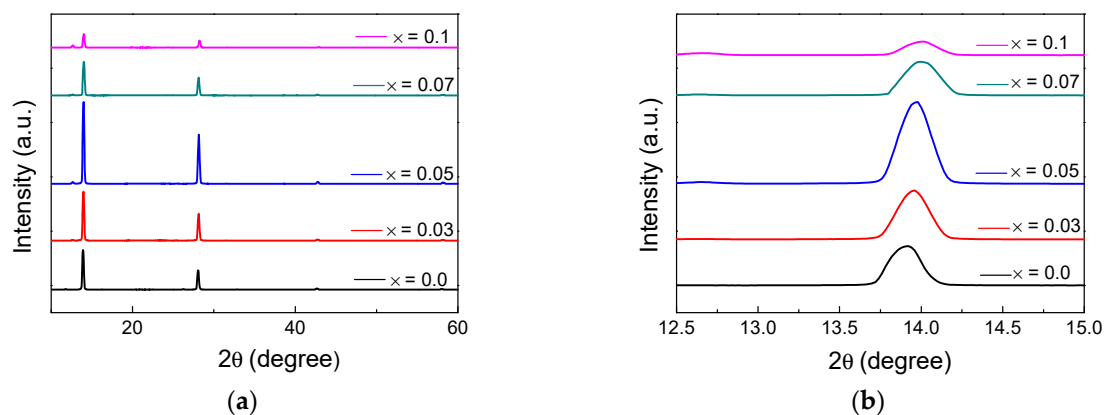
Figure 2. Crystal structure of $(FAPbI_3)_{1-x}(MAPbBr_3)_x$ films. (**a**) XRD patterns for different composition ratios (x = 0, 0.03, 0.05, 0.07, and 0.01) and (**b**) XRD patterns in the 13.0–15.0° range.

Figure 2b shows that as the content of $(MAPbBr_3)_x$ increased, the peak shifted to a high diffraction angle. This shows that the perovskite films were successfully formed, as lattice shrinkage is expected to occur when FA^+ (2.79 Å) is replaced with MA^+ (2.70 Å) [35]. Moreover, additional lattice shrinkage is expected when Br^- (1.96 Å) replaces I^- (2.2 Å), which shifts the corresponding peak to high diffraction angles [32,36].

The results shown in Figure 2 demonstrate that when mixed cation–halide perovskites were prepared, the content of δ-$FAPbI_3$ decreased compared to that of the pure $FAPbI_3$, and the phase stability improved. In particular, the crystallinity of $(FAPbI_3)_{0.95}(MAPbBr_3)_{0.05}$ was the highest among the synthesized samples. However, when more than 7 mol% $MAPbBr_3$ was added, a decrease in crystallinity, owing to the formation of a residue, was observed. This indicates that the overall crystallinity varies depending on the composition of the mixed cation perovskite.

Figure 3 displays SEM images of the $(FAPbI_3)_{1-x}(MAPbBr_3)_x$ perovskite films; it confirms that a change in the composition ratio x affects the film surface. The average diameter lengths of the grain of $(FAPbI_3)_{1-x}(MAPbBr_3)_x$ films (x = 0, 0.03, 0.05, 0.07, 0.1) were 1.629, 1.496, 1.465, 0.922, and 0.815 um. In Figure 3a–c, the grain size decreased as x increased. This is because MA^+ (2.70 Å) has a smaller particle size than FA^+ (2.79 Å), and Br^- (1.96 Å) has a smaller particle size than I^- (2.2 Å) [32,35]; as such, when x increases, more MA^+ and Br^- replace FA^+ and I^- [36]. However, compared to when x = 0.07, the difference in the small grain diameter increase was not significant.

Figure 3d,e show the sharply reduced grain size. Additionally, a residue was observed when x = 0.1 because a portion of $MAPbBr_3$ was decomposed, at because of the high annealing temperature of 150 °C, forming PbI_2 and $PbBr_2$. This suggests that the perovskite was not well-formed at this composition ratio. A small grain size with many crystals observed on the surface leads to deterioration of performance. As residues are produced and replaced with smaller ions, resulting in a smaller grain size, the mobility of carrier transport decreases, which, in turn, increases carrier scattering, leading to poor performance [37].

Figure 4a presents the optical absorption spectra of the $(FAPbI_3)_{1-x}(MAPbBr_3)_x$ films (x = 0, 0.03, 0.05, 0.07, and 0.1). All $(FAPbI_3)_{1-x}(MAPbBr_3)_x$ samples displayed a strong absorbance at 200–500 nm. This demonstrates that the $(FAPbI_3)_{1-x}(MAPbBr_3)_x$-based photodetector sufficiently detected light in the UVC region. The absorbance increased as the value of x increased but decreased when the value of x exceeded 0.07. This suggests that certain $(FAPbI_3)_{1-x}(MAPbBr_3)_x$ compositions (x = 0.03 and 0.05) have better light absorption characteristics than pure $FAPbI_3$.
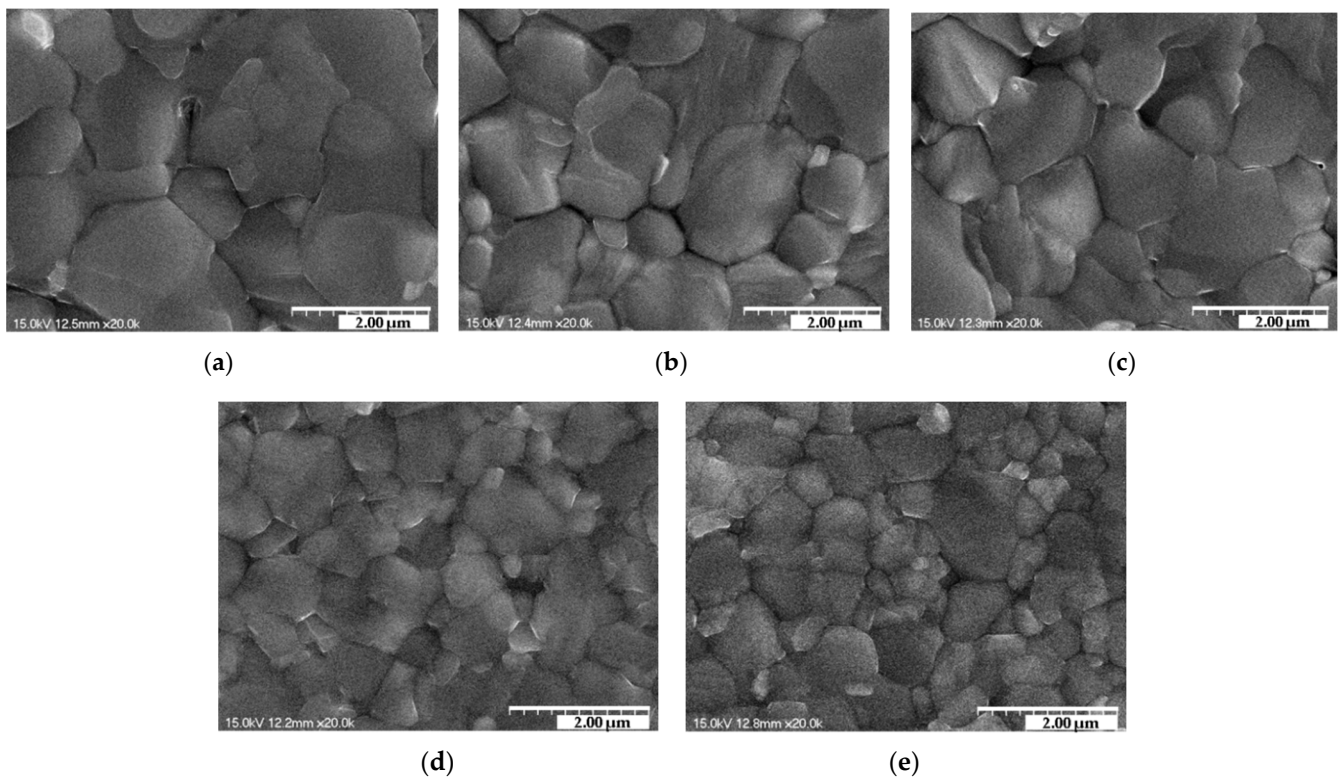
Figure 3. SEM images of $(FAPbI_3)_{1-x}(MAPbBr_3)_x$ films for different composition ratios: (**a**) x = 0, (**b**) x = 0.03, (**c**) x = 0.05, (**d**) x = 0.07, and (**e**) x = 0.1.

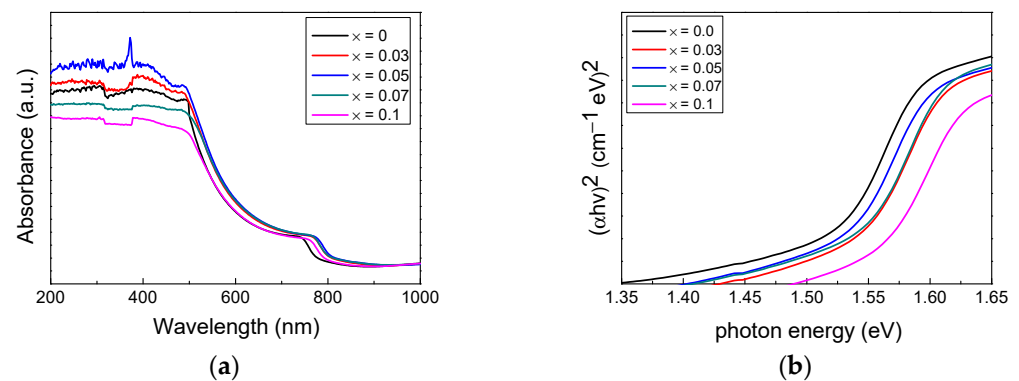**Figure 4.** Light absorption and bandgap of $(FAPbI_3)_{1-x}(MAPbBr_3)_x$ films (x = 0, 0.03, 0.05, 0.07, and 0.01). (**a**) UV-vis absorbance spectra and (**b**) Tauc plot.

Figure 4b is an estimated Tauc plot based on the light absorption of the $(FAPbI_3)_{1-x}(MAPbBr_3)_x$ (x = 0, 0.03, 0.05, 0.07, and 0.1) films. The sharp band energies indicate the presence of a direct bandgap. Semiconductors with wide bandgaps can absorb and emit high-energy photons, enabling the fabrication of high-performance photonic devices, including UV detectors [38]. Based on the light absorption characteristics, the bandgap of pure $FAPbI_3$ and $(FAPbI_3)_{1-x}(MAPbBr_3)_x$ (x = 0.03, 0.05, and 0.07) was estimated to be 1.45 eV and 1.52 eV, respectively. The increase in the band gap was due to the structural distortion caused by the stress on the Pb–I bond resulting from the incorporation of Br [36]. Changes in the kinetic energy of the electron-hole pairs due to Coulomb interactions also result in bandgap differences [39]. The largest bandgap of 1.55 eV was observed when x = 0.1. However, PbI_2 residues are likely to be present when x = 0.1 [36].

Figure 5a shows the electrical properties (resistivity, mobility, and carrier concentration) of the $(FAPbI_3)_{1-x}(MAPbBr_3)_x$ thin films (x = 0, 0.03, 0.05, 0.07, and 0.1). The resistivity of

$(FAPbI_3)_{1−x}(MAPbBr_3)_x$ decreased as the x value increased, except for x = 0.1. In particular, $(FAPbI_3)_{0.95}(MAPbBr_3)_{0.05}$ displayed the lowest resistivity, i.e., 0.00157 Ω cm.
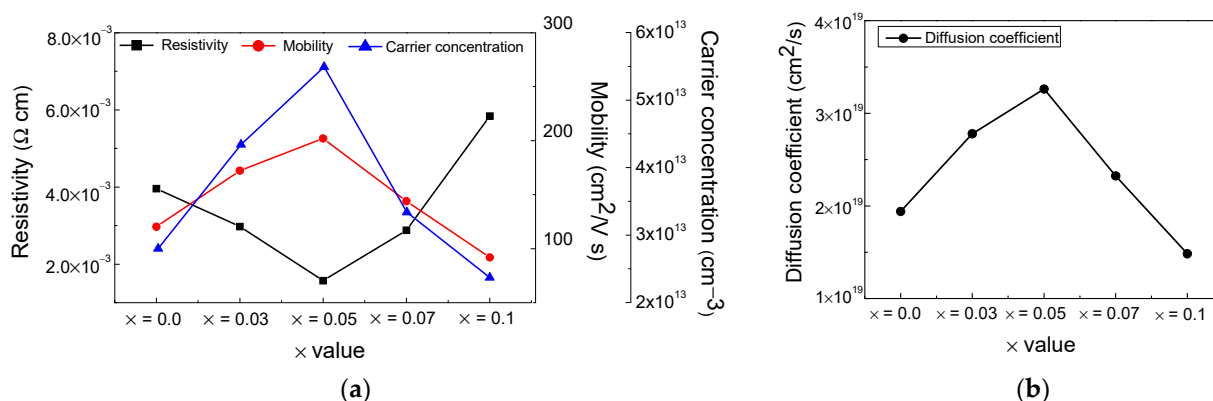

Figure 5. (**a**) Comparison of electrical characteristics including resistivity, carrier concentration and mobility, (**b**) diffusion coefficients of $(FAPbI_3)_{1−x}(MAPbBr_3)_x$ films (x = 0, 0.03, 0.05, 0.07, and 0.01).

Carrier concentration and mobility are significant parameters for semiconductor materials and electronic power devices [40]. All $(FAPbI_3)_{1−x}(MAPbBr_3)_x$ films had carrier concentration values higher than 10^{13} cm$^{−3}$. The current depends on the mobility; the higher the mobility, the higher the current [38,41,42]. The mobilities of the $(FAPbI_3)_{1−x}(MAPbBr_3)_x$ films were 120.3, 172.2, 202.2, 144, and 91.9 cm^2/V.s for x values of 0, 0.03, 0.05, 0.07, and 0.1, respectively.

Figure 5b shows the diffusion coefficient (*D*) of the $(FAPbI_3)_{1−x}(MAPbBr_3)_x$ films (x = 0, 0.03, 0.05, 0.07, and 0.1). *D* is related to the mobility, as shown in Figure 5a. Diffusion involves the movement of charge carriers driven by a concentration gradient [14,43]. In the presence of a magnetic field, *D* is defined using the Einstein relation $D = μKT/q$, where μ is mobility, K is the Boltzmann constant, *T* is the temperature of the sample, and *q* is the amount of charge [43]. The *D* of the $(FAPbI_3)_{1−x}(MAPbBr_3)_x$ films increased as the x value increased, except for x = 0.1. The charge carrier L_D was calculated as $L_D = \sqrt{Dτ}$, where τ is the lifetime [44]. The mobility and L_D are proportional, and high mobility leads to an increase in the *D* and L_D values. When I$^−$ is replaced by Br$^−$, the lattice parameters shrink, leading to an increase in the photogenerated carrier lifetime and the charge carrier mobility [33,45]. Combining the results in Figure 5, it shows that the $(FAPbI_3)_{1−x}(MAPbBr_3)_x$ film had the best electrical properties such as carrier concentration and mobility when x = 0.05.

In addition, to analyze the performance of the $(FAPbI_3)_{1−x}(MAPbBr_3)_x$ (x = 0, 0.03, 0.05, 0.07, and 0.1) photodetectors, the current-voltage (*I–V*) characteristics were measured from −2 V to 2 V at a scan rate of 0.1 V. Measurements were performed in a dark environment and under a 254 nm light source with an output of 0.6 mW/cm^2. In the perovskite photodetector, a Schottky barrier formed owing to the contact with the ITO electrode, and the current flowed through it.

Figure 6a–e show that the $(FAPbI_3)_{1−x}(MAPbBr_3)_x$ photodetectors were barely able to detect 254 nm light at 0.6 mW/cm^2 in a dark environment. However, the $(FAPbI_3)_{0.95}(MAPbBr_3)_{0.05}$ photodetector generated significant photocurrents of −5.61 μA at −2 V and 4.2 μA at 2 V under 254 nm irradiation with an output of 0.6 mW/cm^2, as shown in Figure 6c.
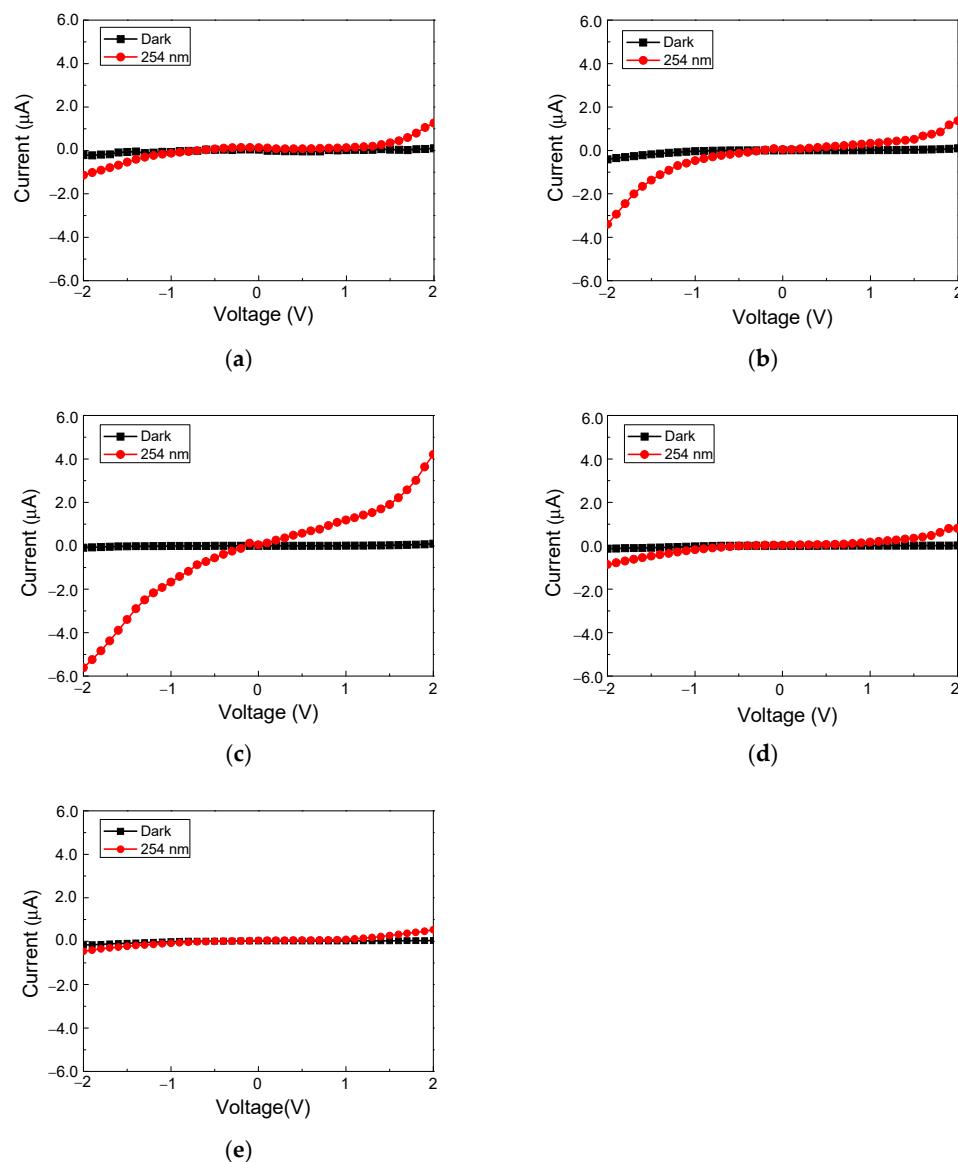
Figure 6. Current–voltage characteristics of $(FAPbI_3)_{1-x}(MAPbBr_3)_x$ photodetectors for different composition ratios: (**a**) x = 0, (**b**) x = 0.03, (**c**) x = 0.05, (**d**) x = 0.07, and (**e**) x = 0.1.

To evaluate the performance of the photodetector, the significant parameters of the detector under a light of 254 nm with an output of 0.6 mW/cm^2 were investigated. Figure 7a shows the responsivity (*R*) of the films. *R* is the main parameter that indicates the performance of the photodetector and the response of the device to the irradiated light. *R* is defined as $R = (I_{254} - I_{dark})/P \times S$ mA/W [14], where I_{254} is the current when irradiated with 254 nm light, I_{dark} is the dark environment current, *P* is the power of the incident light, and *S* is the irradiated area of the device [46]. *R* gradually decreased as the bias decreased owing to the change in the photon-charge conversion efficiency of the photodetector [10]. Under 254 nm illumination, with an output of 0.6 mW/cm^2, the *R* values of $(FAPbI_3)_{1-x}(MAPbI_3)_x$ were 0.85, 2.77, 5.07, 0.68, and 0.26 mA/W at −2 V when x was 0, 0.03, 0.05, 0.07, and 0.1, respectively.
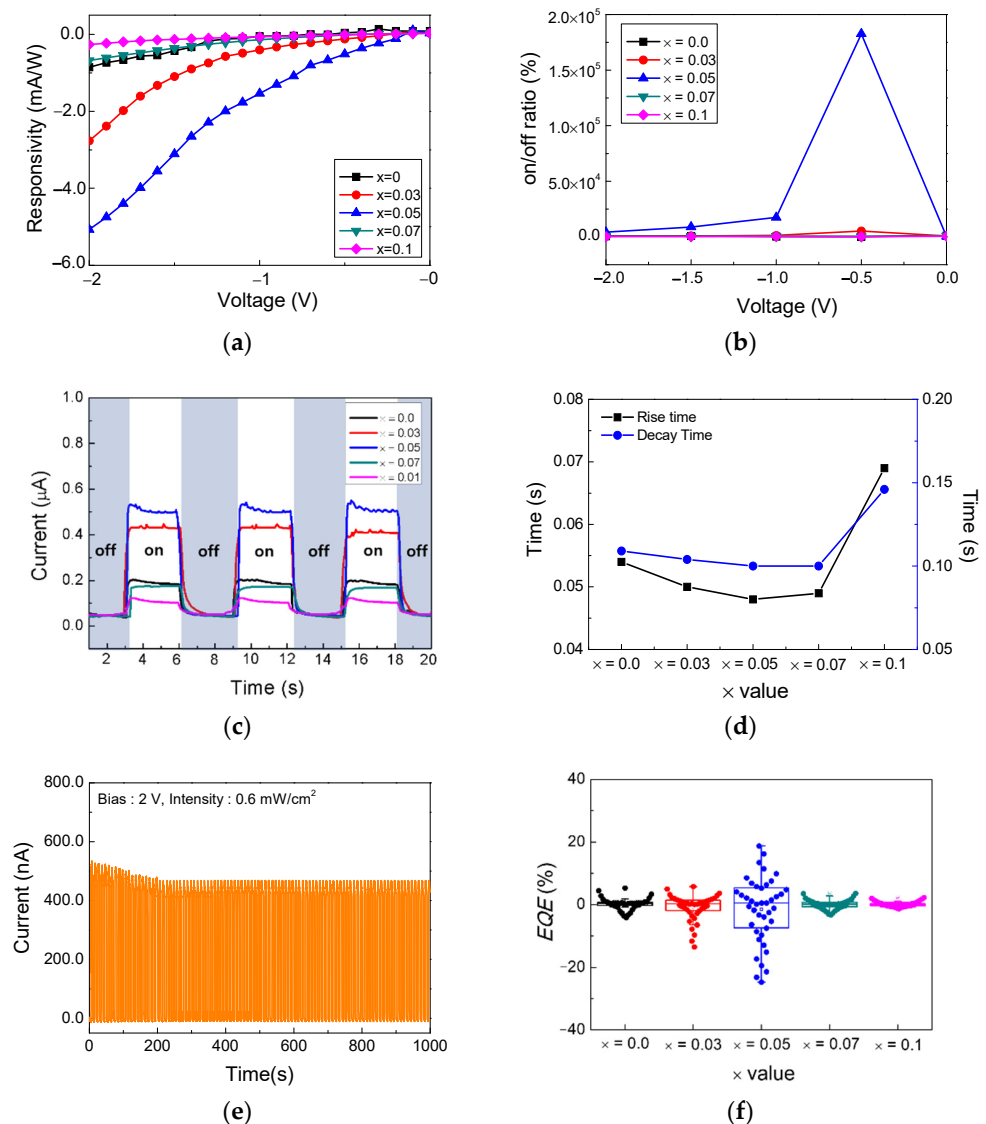
Figure 7. $(FAPbI_3)_{1-x}(MAPbBr_3)_x$ photodetector response. (**a**) Responsivity curves, (**b**) on/off ratio, (**c**) transient photo-responses, (**d**) rise and decay times, (**e**) photostability of the prepared device switching under the illumination of 254 nm light with an intensity of 0.6 mW/cm^2, and (**f**) external quantum efficiency.

Figure 7b shows the on/off ratios of the $(FAPbI_3)_{1-x}(MAPbBr_3)_x$ photodetectors in the reverse bias region from -2 V to 0 V. A high on/off ratio is related to good performance in a photodetector [11]. The on/off ratios at -2 V were 539, 835, 4211, 663, and 258% for x = 0, 0.03, 0.05, 0.07, and 0.1, respectively. Additionally, when the voltage was -0.5 V, the largest on/off ratio was observed for x = 0.05.

Figure 7c,d show the time dependent response of the $(FAPbI_3)_{1-x}(MAPbBr_3)_x$ photodetectors. An on/off switching test was performed to observe transient photoresponses under 254 nm radiation with an 0.6 mA/cm^2 intensity at a 2 V bias. Response times, such as rise and decay times, could be inferred from the relative speed of response of the detector to changes in the optical signal. Figure 7c shows that during on/off switching, the $(FAPbI_3)_{1-x}(MAPbBr_3)_x$ (x = 0.03 and 0.05) photodetectors exhibited a higher photoresponse than pure FAPbI$_3$. In addition, Figure 7d shows that when the x value was 0.05, the $(FAPbI_3)_{1-x}(MAPbBr_3)_x$ photodetectors had the smallest rise and decay times, i.e., 0.048 and 0.1 s, respectively. Therefore, the $(FAPbI_3)_{0.95}(MAPbBr_3)_{0.05}$ photodetector had the fastest photo-response among all the photodetectors, and is highly sensitive.

Figure 7e shows the on/off repeatability of the $(FAPbI_3)_{0.95}(MAPbBr_3)_{0.05}$ photodetector. The on/off switch was irradiated for 1000 s using a 254 nm light source with an output of 0.6 mW/cm^2. In the first on/off iteration, the photocurrent was 523 nA. The light was irradiated for 5 s, and the photodetector was cycled on/off 100 times. After 100 cycles, the photocurrent decreased slightly to 468 nA, but remained constant from the 16th cycle to the 100th cycle. Although a slight decrease in photocurrent was observed, the maintenance of the photocurrent over a relatively long time proves its reproducibility.

EQE, which is the number of electrons produced per incident photon, is another important parameter that indicates the detector performance. *EQE* is defined as $Rhc/e\lambda$, where *R* is the responsivity, *h* is the Planck constant, c is the speed of light, e is the electron charge, and λ is the wavelength of the light [9]. Figure 7f shows the *EQE* from −2 V to 2 V bias as a box plot under 254 nm light irradiation with 0.6 mA/cm^2 intensity. Figure 7c shows that the *EQE* increases up to x = 0.05 and decreases at x = 0.07. These results exhibit the same pattern as the other measurements (XRD, UV-vis, and responsivity measurements) and demonstrate that among the $(FAPbI_3)_{1-x}(MAPbBr_3)_x$ (x = 0, 0.03, 0.05, 0.07, and 0.1) photodetectors, the $(FAPbI_3)_{0.95}(MAPbBr_3)_{0.05}$ composition exhibited the best optical properties.

Detectivity *D** is an important photodetector parameter, defined as $D^* = R/(2qJ_{dark})^{1/2}$, where *R* is the responsivity, *q* is the electron charge, and J_{dark} is the current density of the dark current [14,38]. In Table 1, parameters, such as *R*, *D*, and *EQE,* of UVC photodetectors fabricated using various materials are listed. The *R* and *EQE* values of the $(FAPbI_3)_{0.95}(MAPbBr_3)_{0.05}$ photodetector fabricated in this study were superior to those of photodetectors reported in other studies. This suggests that the perovskite-based UVC photodetectors fabricated in this study are promising candidates in the field of UVC sensing, as the perovskites can be fabricated using a simple process at lower temperatures than those of previously reported photodetectors. In addition, the *R* and *EQE* values were superior to those of perovskite-based photodetectors reported in other studies, while the *D** values were similar. These results indicate that $(FAPbI_3)_{0.95}(MAPbBr_3)_{0.05}$ is a promising material for developing perovskite-based photodetectors.

Table 1. Comparison of UVC various photodetector parameters.

Materials	Light (nm)	Bias (V)	R (mA/W)	D* (Jones)	EQE (%)	Ref.
$(FAPbI_3)_{0.95}(MAPbI_3)_{0.05}$	254	−2	5.07	5.49×10^{11}	24.8	[In this study]
$(FAPbI_3)_{1-x}(MAPbBr_3)_x$	254	0	4.92	7.57×10^{10}	-	[11]
$MAPbBr_3$	254	2	4.57	1.02×10^{13}	22.2	[14]
$CsPbBr_{3/}$	254	2	0.24	1.1×10^{9}	0.05	[47]
$CaSnO_3$	255	0	2.25	1.56×10^{10}	1.06	[48]
$Ag/GQD/Au$	254	5	2.1	9.59×10^{11}	10.3	[49]
$Mn_{0.52}Zn_{0.48}O$	250	10	0.1	-	-	[18]
$Nb:SrTiO_3/Ga_2O_3$	254	0	2.6	-	1.3	[7]
$Au/ZnS QDs/Au$	254	40	0.077	-	-	[50]

4. Conclusions

Mixed cation–halide perovskite $(FAPbI_3)_{1-x}(MAPbBr_3)_x$ (x = 0, 0.03, 0.05, 0.07, and 0.1)-based photodetectors were investigated. $(FAPbI_3)_{1-x}(MAPbBr_3)_x$ films exhibited the most improved stability and light absorption when the $MAPbBr_3$ ratio was 5 mol%. The $(FAPbI_3)_{0.95}(MAPbBr_3)_{0.05}$ UVC photodetector exhibited an *EQE* of 24.8%, a mobility of 202.2 cm^2/Vs, a response of 5.07 mA/W, and a detection rate of 5.49×10^{11} Jones. These are excellent parameter values compared with previously reported values for perovskite-based photodetectors fabricated using the solution process. By applying the process described in this study, it is possible to fabricate a photodetector with improved optical properties through a low-energy process. This suggests that mixed cation–halide perovskite-based photodetectors have significant potential for use in UVC photodetectors.

References

1. Leung, S.F.; Ho, K.T.; Kung, P.K.; Hsiao, V.K.; Alshareef, H.N.; Wang, Z.L.; He, J.H. A self-powered and flexible organometallic halide perovskite photodetector with very high detectivity. *Adv. Mater.* **2018**, *30*, 1704611.
2. Li, C.; Ma, Y.; Xiao, Y.; Shen, L.; Ding, L. Advances in perovskite photodetectors. *InfoMat* **2020**, *2*, 1247–1256.
3. Fang, F.; Li, H.; Fang, S.; Zhou, B.; Huang, F.; Ma, C.; Wan, Y.; Jiang, S.; Wang, Y.; Tian, B.; et al. 2D $Cs_2AgBiBr_6$ with Boosted Light–Matter Interaction for High-Performance Photodetectors. *Adv. Opt. Mater.* **2021**, *9*, 2001930.
4. Yang, W.; Chen, J.; Zhang, Y.; Zhang, Y.; He, J.H.; Fang, X. Silicon-compatible photodetectors: Trends to monolithically integrate photosensors with chip technology. *Adv. Funct. Mater.* **2019**, *29*, 1808182.
5. Yao, J.; Yang, G. 2D material broadband photodetectors. *Nanoscale* **2020**, *12*, 454–476.
6. Tsai, S.H.; Basu, S.; Huang, C.Y.; Hsu, L.C.; Lin, Y.G.; Horng, R.H. Deep-ultraviolet photodetectors based on epitaxial $ZnGa_2O_4$ thin films. *Sci. Rep.* **2018**, *8*, 14056. [CrossRef]
7. Guo, D.; Liu, H.; Li, P.; Wu, Z.; Wang, S.; Cui, C.; Li, C.; Tang, W. Zero-power-consumption solar-blind photodetector based on β-Ga_2O_3/NSTO heterojunction. *ACS Appl. Mater. Interfaces* **2017**, *9*, 1619–1628.
8. Park, T.; Hur, J. Self-Powered Low-Cost UVC Sensor Based on Organic-Inorganic Heterojunction for Partial Discharge Detection. *Small* **2021**, *17*, 2100695.
9. Preto, S.; Gomes, C.C. Ultraviolet radiation in sunlight and artificial lighting systems: Are they alike? In *International Conference on Applied Human Factors and Ergonomics*; Springer: Cham, Germany, 2017; pp. 287–298.
10. Nguyen, T.M.H.; Kim, S.; Bark, C.W. Solution-processed and self-powered photodetector in vertical architecture using mixed-halide perovskite for highly sensitive UVC detection. *J. Mater. Chem. A* **2021**, *9*, 1269–1276. [CrossRef]
11. Nguyen, T.M.H.; Lee, S.K.; Kim, S.; Bark, C.W. Practical Demonstration of Deep-Ultraviolet Detection with Wearable and Self-Powered Halide Perovskite-Based Photodetector. *ACS Appl. Mater. Interfaces* **2021**, *13*, 57609–57618.
12. Ertle, D.; Friedl, R.; Vogel, F.; Fantz, U. Experimental Investigation and Modelling of the Spectral Intensity of the N_2-Emission in Argon Low-Pressure Arc Discharges. In Proceedings of the 30th International Conference on Phenomena in Ionized Gases (ICPIG 2011), Belfast, UK, 29 August–2 September 2011; p. D15.
13. Dixon, A.J.; Dixon, B.F. Ultraviolet radiation from welding and possible risk of skin and ocular malignancy. *Med. J. Aust.* **2004**, *181*, 155–157. [CrossRef]
14. Shin, S.G.; Bark, C.W.; Choi, H.W. Study on Performance Improvements in Perovskite-Based Ultraviolet Sensors Prepared Using Toluene Antisolvent and CH_3NH_3Cl. *Nanomaterials* **2021**, *11*, 1000. [CrossRef]
15. Ferreira, S.H.; Cunha, I.; Pinto, J.V.; Neto, J.P.; Pereira, L.; Fortunato, E.; Martins, R. UV-Responsive Screen-Printed Porous ZnO Nanostructures on Office Paper for Sustainable and Foldable Electronics. *Chemosensors* **2021**, *9*, 192. [CrossRef]
16. Claro, P.I.; Marques, A.C.; Cunha, I.; Martins, R.F.P.; Pereira, L.M.; Marconcini, J.M.; Mattoso, L.H.C.; Fortunato, E. Tuning the electrical properties of cellulose nanocrystals through laser-induced graphitization for UV photodetectors. *ACS Appl. Nano Mater.* **2021**, *4*, 8262–8272. [CrossRef]
17. Figueira, J.; Gaspar, C.; Carvalho, J.T.; Loureiro, J.; Fortunato, E.; Martins, R.; Pereira, L. Sustainable fully printed UV sensors on cork using zinc oxide/ethylcellulose inks. *Micromachines* **2019**, *10*, 601. [CrossRef]
18. Ju, Z.G.; Shan, C.X.; Jiang, D.Y.; Zhang, J.Y.; Yao, B.; Zhao, D.X.; Shen, D.Z.; Fan, X.W. Mg_xZn_{1-x}O-based photodetectors covering the whole solar-blind spectrum range. *Appl. Phys. Lett.* **2008**, *93*, 173505. [CrossRef]
19. Gu, S.; Lin, R.; Han, Q.; Gao, Y.; Tan, H.; Zhu, J. Tin and mixed lead–tin halide perovskite solar cells: Progress and their application in tandem solar cells. *Adv. Mater.* **2020**, *32*, 1907392. [CrossRef]
20. Bibi, A.; Lee, I.; Nah, Y.; Allam, O.; Kim, H.; Quan, L.N.; Tang, J.; Walsh, A.; Jang, S.S.; Sargent, E.H.; et al. Lead-free halide double perovskites: Toward stable and sustainable optoelectronic devices. *Mater. Today* **2021**, *49*, 123–144. [CrossRef]
21. Li, Y.; Shi, Z.F.; Li, X.J.; Shan, C.X. Photodetectors based on inorganic halide perovskites: Materials and devices. *Chin. Phys. B* **2019**, *28*, 017803. [CrossRef]

22. Imran, M.; Khan, N.A. Perovskite phase formation in formamidinium–methylammonium lead iodide bromide $(FAPbI_3)_{1-x}(MAPbBr_3)_x$ materials and their morphological, optical and photovoltaic properties. *Appl. Phys. A* **2019**, *125*, 575. [CrossRef]

23. Tong, G.; Li, H.; Zhu, Z.; Zhang, Y.; Yu, L.; Xu, J.; Jiang, Y. Enhancing hybrid perovskite detectability in the deep ultraviolet region with down-conversion dual-phase $(CsPbBr_3–Cs_4PbBr_6)$ films. *J. Phys. Chem. Lett.* **2018**, *9*, 1592–1599. [CrossRef]

24. Guo, X.; Ngai, K.; Qin, M.; Lu, X.; Xu, J.; Long, M. The compatibility of methylammonium and formamidinium in mixed cation perovskite: The optoelectronic and stability properties. *Nanotechnology* **2020**, *32*, 075406. [CrossRef]

25. Zhou, D.; Zhou, T.; Tian, Y.; Zhu, X.; Tu, Y. Perovskite-based solar cells: Materials, methods, and future perspectives. *J. Nanomater.* **2018**, *2018*, 8148072. [CrossRef]

26. Ava, T.T.; Al Mamun, A.; Marsillac, S.; Namkoong, G. A review: Thermal stability of methylammonium lead halide based perovskite solar cells. *Appl. Sci.* **2019**, *9*, 188. [CrossRef]

27. Reyna, Y.; Salado, M.; Kazim, S.; Perez-Tomas, A.; Ahmad, S.; Lira-Cantu, M. Performance and stability of mixed $FAPbI_{3(0.85)}MAPbBr_{3(0.15)}$ halide perovskite solar cells under outdoor conditions and the effect of low light irradiation. *Nano Energy* **2016**, *30*, 570–579. [CrossRef]

28. Li, W.G.; Rao, H.S.; Chen, B.X.; Wang, X.D.; Kuang, D.B. A formamidinium–methylammonium lead iodide perovskite single crystal exhibiting exceptional optoelectronic properties and long-term stability. *J. Mater. Chem. A* **2017**, *5*, 19431–19438. [CrossRef]

29. Lee, J.W.; Seol, D.J.; Cho, A.N.; Park, N.G. High-efficiency perovskite solar cells based on the black polymorph of HC $(NH_2)_2PbI_3$. *Adv. Mater.* **2014**, *26*, 4991–4998. [CrossRef]

30. Wang, M.; Cao, F.; Deng, K.; Li, L. Adduct phases induced controlled crystallization for mixed-cation perovskite solar cells with efficiency over 21%. *Nano Energy* **2019**, *63*, 103867. [CrossRef]

31. Chen, L.; Cao, H.; Wang, S.; Luo, Y.; Tao, T.; Sun, J.; Zhang, M. Efficient air-stable perovskite solar cells with a $(FAI)_{0.46}(MAI)_{0.40}$ $(MABr)_{0.14}(PbI_2)_{0.86}(PbBr_2)_{0.14}$ active layer fabricated via a vacuum flash-assisted method under RH > 50%. *RSC Adv.* **2019**, *9*, 10148–10154. [CrossRef]

32. Tang, S.; Xiao, X.; Hu, J.; Gao, B.; Chen, H.; Zuo, Z.; Qi, Q.; Peng, Z.; Wen, J.; Zou, D. Mechanochemical synthesis of pure phase mixed-cation/anion $(FAPbI_3)_x(MAPbBr_3)_{1-x}$ hybrid perovskite materials: Compositional engineering and photovoltaic performance. *RSC Adv.* **2021**, *11*, 5874–5884. [CrossRef]

33. Tumusange, M.S.; Subedi, B.; Chen, C.; Junda, M.M.; Song, Z.; Yan, Y.; Podraza, N.J. Impact of Humidity and Temperature on the Stability of the Optical Properties and Structure of $MAPbI_3$, $MA_{0.7}FA_{0.3}PbI_3$ and $(FAPbI_3)_{0.95}(MAPbBr_3)_{0.05}$ Perovskite Thin Films. *Materials* **2021**, *14*, 4054. [CrossRef] [PubMed]

34. Xu, F.; Zhang, T.; Li, G.; Zhao, Y. Mixed cation hybrid lead halide perovskites with enhanced performance and stability. *J. Mater. Chem. A* **2017**, *5*, 11450–11461. [CrossRef]

35. Li, X.; Yang, J.; Jiang, Q.; Chu, W.; Zhang, D.; Zhou, Z.; Ren, Y.; Xin, J. Enhanced photovoltaic performance and stability in mixed-cation perovskite solar cells via compositional modulation. *Electrochim. Acta* **2017**, *247*, 460–467. [CrossRef]

36. Atourki, L.; Vega, E.; Marí, B.; Mollar, M.; Ahsaine, H.A.; Bouabid, K.; Ihlal, A. Role of the chemical substitution on the structural and luminescence properties of the mixed halide perovskite thin $MAPbI_{3-x}Br_x$ ($0 \leq x \leq 1$) films. *Appl. Surf. Sci.* **2016**, *371*, 112–117. [CrossRef]

37. Chen, L.C.; Tseng, Z.L.; Huang, J.K.; Chen, C.C.; Chang, S.H. Fullerene-based Electron transport layers for semi-transparent MAPbBr3 perovskite films in planar perovskite solar cells. *Coatings* **2016**, *6*, 53. [CrossRef]

38. Zou, Y.; Zhang, Y.; Hu, Y.; Gu, H. Ultraviolet detectors based on wide bandgap semiconductor nanowire: A review. *Sensors* **2018**, *18*, 2072. [CrossRef]

39. Mosconi, E.; Amat, A.; Nazeeruddin, M.K.; Gratzel, M.; De Angelis, F. First-principles modeling of mixed halide organometal perovskites for photovoltaic applications. *J. Phys. Chem. C* **2013**, *117*, 13902–13913. [CrossRef]

40. Koizumi, S.; Umezawa, H.; Pernot, J.; Suzuki, M. 2-Doping and Semiconductor Characterizations. In *Power Electronics Device Applications of Diamond Semiconductors*; Woodhead Publishing: Sawston, UK, 2018; pp. 99–189.

41. Bercegol, A.; Ory, D.; Suchet, D.; Cacovich, S.; Fournier, O.; Rousset, J.; Lombez, L. Quantitative optical assessment of photonic and electronic properties in halide perovskite. *Nat. Commun.* **2019**, *10*, 1586. [CrossRef]

42. Myronov, M. Molecular Beam Epitaxy of High Mobility Silicon, Silicon Germanium and Germanium Quantum Well Heterostructures. In *Molecular Beam Epitaxy*; Elsevier: Amsterdam, The Netherlands, 2018; pp. 37–54.

43. Hodes, G.; Kamat, P.V. Understanding the implication of carrier diffusion length in photovoltaic cells. *J. Phys. Chem. Lett.* **2015**, *6*, 4090–4092. [CrossRef]

44. Li, Y.; Yan, W.; Li, Y.; Wang, S.; Wang, W.; Bian, Z.; Xiao, L.; Gong, Q. Direct observation of long electron-hole diffusion distance in $CH_3NH_3PbI_3$ perovskite thin film. *Sci. Rep.* **2015**, *5*, 14485. [CrossRef]

45. Lin, C.; Li, S.; Zhang, W.; Shao, C.; Yang, Z. Effect of bromine substitution on the ion migration and optical absorption in $MAPbI_3$ perovskite solar cells: The first-principles study. *ACS Appl. Energy Mater.* **2018**, *1*, 1374–1380. [CrossRef]

46. Chen, J.H.; Jing, Q.; Xu, F.; Lu, Y.Q. High-sensitivity optical-fiber-compatible photodetector with an integrated $CsPbBr_3$–graphene hybrid structure. *Optica* **2017**, *4*, 835–838. [CrossRef]

47. Zhang, T.; Wang, F.; Zhang, P.; Wang, Y.; Chen, H.; Li, J.; Wu, J.; Chen, L.; Chen, Z.D.; Li, S. Low-temperature processed inorganic perovskites for flexible detectors with a broadband photoresponse. *Nanoscale* **2019**, *11*, 2871–2877. [CrossRef] [PubMed]

48. Tran, M.H.; Park, T.; Hur, J. Wide-bandgap $CaSnO_3$ perovskite as an efficient and selective deep-UV absorber for self-powered and high-performance pin photodetector. *ACS Appl. Mater. Interfaces* **2021**, *13*, 13372–13382. [CrossRef]

49. Zhang, Q.; Jie, J.; Diao, S.; Shao, Z.; Zhang, Q.; Wang, L.; Deng, W.; Hu, W.; Xia, H.; Yuan, X.; et al. Solution-processed graphene quantum dot deep-UV photodetectors. *ACS Nano* **2015**, *9*, 1561–1570. [CrossRef]

50. Xia, Y.; Zhai, G.; Zheng, Z.; Lian, L.; Liu, H.; Zhang, D.; Gao, J.; Zhai, T.; Zhang, J. Solution-processed solar-blind deep ultraviolet photodetectors based on strongly quantum confined ZnS quantum dots. *J. Mater. Chem. C* **2018**, *6*, 11266–11271. [CrossRef]